



# Implementation of a high order lattice spring model for elasticity

Shuan-Feng Zhao<sup>a,c</sup>, Gao-Feng Zhao<sup>b,\*</sup>

<sup>a</sup> School of Mechanical Engineering, Xi'an Jiaotong University, Xi'an, China

<sup>b</sup> School of Civil and Environmental Engineering, The University of New South Wales, Sydney, NSW 2052, Australia

<sup>c</sup> School of Mechanical Engineering, Xi'an University of Science and Technology, Xi'an, China

## ARTICLE INFO

### Article history:

Received 12 January 2012

Received in revised form 3 May 2012

Available online 30 May 2012

### Keywords:

High order  
Lattice spring model  
Elasticity

## ABSTRACT

In a lattice spring model (LSM), the material is discretised into particles linked by springs. However, LSMs always adopt linear springs, which results in a stiff approximation of the corresponding elastic solution. In this work, a high order LSM is proposed to overcome this limitation by introducing additional degrees of freedoms (DOFs) to the particles. Based on the energy minimisation principle and the local strain technique, equations for the stiffness matrices of high order LSM are derived. Relationships between micro spring parameters and macro material constants are derived from the Cauchy-born rules and the hyper-elastic theory. Numerical examples show that the high order LSM can provide a better solution than that of the linear LSM and that the LSM is more suitable for modelling singularity and fracture problems.

© 2012 Elsevier Ltd. All rights reserved.

## 1. Introduction

Hrennikoff (1941) proved that a regular triangular lattice of bars (springs) is capable of solving problems of continuum elasticity with Poisson's ratio fixed at  $1/3$ . This observation is regarded as the origin of the lattice spring model (LSM). The LSM has had little success due to computational limitations and the subsequent development of the Finite Element Method (FEM). However, in recent years, researchers have renewed their interests in LSMs as these models are very suitable for fracturing simulations of solids by either simply removing connecting elements that exceed the strength or successively degrading their mechanical properties according to cohesive laws (e.g., Hahn et al., 2010; Darve and Nicot, 2005; Cui et al., 2011; Wang et al., 2009). Molecular Dynamics (MD) is a notable numerical method to model micromechanics of discrete systems, which was applied to study the failure mechanism of micro granular material (Farkas et al., 2002; Hasnaoui et al., 2003) and propagation of mode-I crack in the quasi-crystal material (Rosch et al., 2005). However, due to the computational limitation, MD is inadequate to handle some engineering problems such as the mechanical behavior of granular material. Inspired from MD, Cundall and Strack (1979) developed the Discrete Element Method (DEM) to tackle the problem. In DEM, atoms were replaced by rock grains and potential function was simplified as contact law. These simplifications have been proven as very successful at study the mechanical response of granular materials (e.g., Williams and Mustoe, 1987; Yu, 2004). Since dynamic relax-

ation is usually adopted in DEM, it is still computational cost for static or quasi static analysis. In the past few decades, a family of methods coined as lattice spring models (LSMs) have been developed. These LSMs have the following common characteristics: (a) the solid is discretised into particles, which are connected through spring-type forces; (ii) the macro-mechanical response is derived from the microscopic interactions between particles; (iii) the material failure at the continuous level is captured naturally from the spring failure at the micro-discontinuous level; (iv) complex constitutive relationships and contact mechanisms are readily implemented; and (v) the system equations are solved directly, and static problem can be solved through one step. Due to its discrete nature, LSM has successfully been used to investigate crack formation and propagation in heterogeneous materials (e.g., Ostojja-Starzewski et al., 1977; Lilliu and van Mier, 2003; Kozicki, 2007).

The most significant development of LSM is the model proposed by Heermann et al. (1989), in which the springs were replaced with beam elements. This model introduces additional rotational Degrees of Freedom (DOF) on each particle and can be viewed as the discretisation of a micropolar continuum. The model has been further developed for modelling concrete fractures (e.g., Schlungen and Garboczi, 1997; Lilliu and van Mier, 2003). Another development of LSM is the polygon-based lattice models, which were developed by subdividing the material into particles with a general shape and then connecting them along their boundaries through normal and shear springs (Mustoe, 1992; Cusatis et al., 2003). The purpose of introducing rotational DOFs into LSM is to enable it to represent different Poisson's ratios. The Poisson's ratio restriction was also overcome by introducing non-central force interactions (shear springs) between particles. For example, Hassold and Srolovitz (1989) proposed a harmonic potential for the rotation

\* Corresponding author. Tel.: +61 2 9385 6139; fax: +61 2 9385 5022.

E-mail address: [gaofeng.zhao@unsw.edu.au](mailto:gaofeng.zhao@unsw.edu.au) (G.-F. Zhao).

of bonds from their initial orientation, and Caldarelli et al. (1999) and Parisi and Caldarelli (2000) developed a non-central two-body interaction limiting the rotational freedom of bonds to modify Poisson's ratio. However, it was found that it is necessary to consider the particle-scale rotational DOFs for the LSM to obtain a realistic fracture pattern (Wang et al., 2006, Potyondy and Cundall, 2004). Adding the rotational DOFs will not only increase the total DOFs of the model but also make the implementation complex. Recently, this dilemma has been solved using the Distinct Lattice Spring Model (DLSM) (Zhao, 2010; Zhao et al., 2011), in which the particle rotation was considered by using a local strain calculation technique. The DLSM does not require rotational DOFs but is still able to predict correct fracture patterns and various Poisson's ratios (e.g., Zhao et al., 2011; Kazerani et al., 2010; Ma et al., 2011).

In addition to solving the Poisson's ratio limitation, other improvements of LSM were also developed by researchers. For example, O'Brien (2008) implemented visco-elastic springs into LSM to simulate seismic wave propagation in visco-elastic media, Kazerani et al. (2010) developed a full rate-dependent cohesive law for the dynamic cracking problem, and Buxton et al. (2001) developed a plastic LSM for plastic problems. The LSM has also been developed to solve multi-physics problems. For example, Cook et al. (2004) and Sakaguchi and Muhlhaus (2000) developed a coupled fluid flow and mechanical deformation LSM, and Kwapińska and Saage (2008) and Hahn et al. (2011) applied LSMs for thermal problems. However, compared with the development of FEM, e.g., the Partition Unity Method (PUM) (Babuska and Melenk, 1997) and eXtend Finite Element Method (XFEM) (Belytschko and Black, 1999), the LSM remains an underdeveloped method. For example, classical LSMs always adopt linear springs, which will result in a stiff approximation of the corresponding elastic solution. In this paper, a high order LSM is developed based on the DLSM (Zhao, 2010; Zhao et al., 2011). Firstly, the basic principle and formulations of the DLSM are introduced. Then, the proposed high order LSM and associated numerical techniques are described. The high order LSM is validated by numerical simulations of elastic problems and comparisons with linear DLSM and FEM solutions. Finally, the influence of lattice size, lattice type, high order sub spring layout and fracture simulation are also studied.

## 2. Distinct Lattice Spring Model

The most distinct feature of DLSM (Zhao, 2010; Zhao et al., 2011) is its ability to evaluate spring deformation by using the local strain technique rather than the particle displacements. This

technique makes the model rotationally invariant and allows one to overcome the restriction on Poisson's ratio in classical LSMs. For a two-dimensional DLSM, the lattice network can be represented by edges of a triangular FEM mesh (see Fig. 1a). The normal and shear deformation of the bond were calculated from the local strain of the bond:

$$\bar{\mathbf{u}} = \mathbf{T}\mathbf{s} \quad (1)$$

where  $\bar{\mathbf{u}} = (\bar{u}^n, \bar{u}^s)^T$  is the normal and shear deformation vector of the bond,  $\mathbf{T}$  is the transform matrix, which is given as

$$\mathbf{T} = l \begin{bmatrix} n_x^2 & n_y^2 & 2n_x n_y \\ -n_x n_y & n_x n_y & n_x^2 - n_y^2 \end{bmatrix} \quad (2)$$

Here,  $l$  is the length of the spring,  $n_x$  and  $n_y$  are components of the normal vector of the bond, and  $\mathbf{s} = [\varepsilon_{xx}, \varepsilon_{yy}, \varepsilon_{xy}]^T$  is the strain vector composed of the three strain components, which can be calculated as

$$\mathbf{s} = \mathbf{B}\mathbf{u} \quad (3)$$

where  $\mathbf{B}$  is the interpolation matrix, which can be obtained from the FEM interpolation or moving least squares (MLS) procedure (Zhao, 2010), and  $\mathbf{u}$  is the displacement vector of the particles involved. It should be mentioned that Eq. (1) is equivalent to the relative displacement between two particles. A proof is given in Appendix A.

The global stiffness matrix is assembled by the element stiffness matrix contributed by each bond, which can be obtained from the energy minimisation principle. Firstly, the strain energy stored in each bond is

$$\Pi_b = \frac{1}{2} \bar{\mathbf{u}}^T \mathbf{K}_{\text{bond}} \bar{\mathbf{u}} \quad (4)$$

where  $\mathbf{K}_{\text{bond}}$  is the bond stiffness matrix at the local coordinate:

$$\mathbf{K}_{\text{bond}} = \begin{bmatrix} k_n & 0 \\ 0 & k_s \end{bmatrix} \quad (5)$$

where  $k_n$  is the normal stiffness and  $k_s$  is the shear stiffness. According to Eqs. (1)–(5), the total energy in the bond can be written as

$$\Pi = \Pi_b - \Pi_f = \frac{1}{2} (\mathbf{T}\mathbf{B}\mathbf{u})^T \mathbf{K}_{\text{bond}} (\mathbf{T}\mathbf{B}\mathbf{u}) - \mathbf{f}\mathbf{u}^T \quad (6)$$

where  $\Pi_f$  is the virtual work done by the external force, and  $\mathbf{f}$  is the force vector of the particles.

According to energy minimisation principle

$$\frac{\partial \Pi}{\partial u_i} = (\mathbf{T}\mathbf{B})^T \mathbf{K}_{\text{bond}} (\mathbf{T}\mathbf{B}\mathbf{u}) - \mathbf{f} = 0 \quad (7)$$

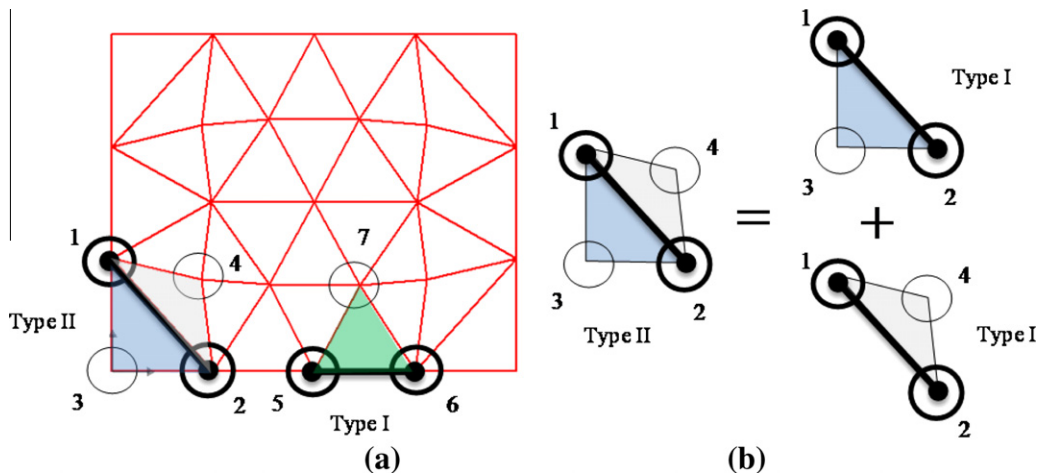


Fig. 1. LSM representation of a solid by FEM mesh (a) lattice model, (b) two types of bonds.

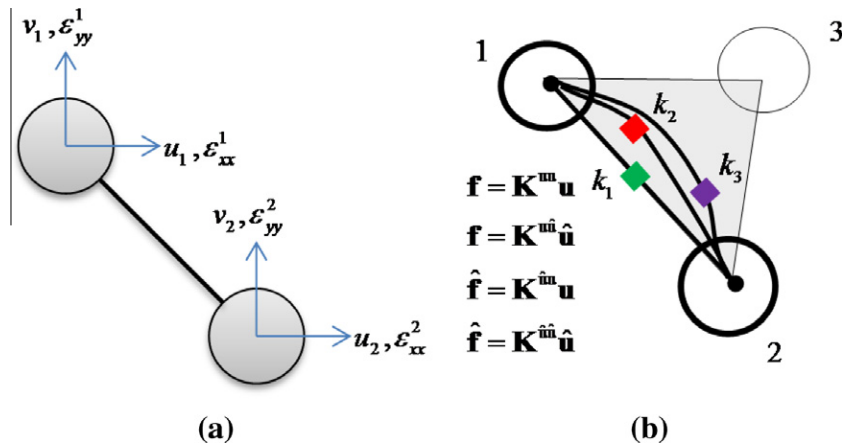


Fig. 2. High order spring for LSM (a) particles with general DOFs linked with high order spring, (b) layout of sub springs.

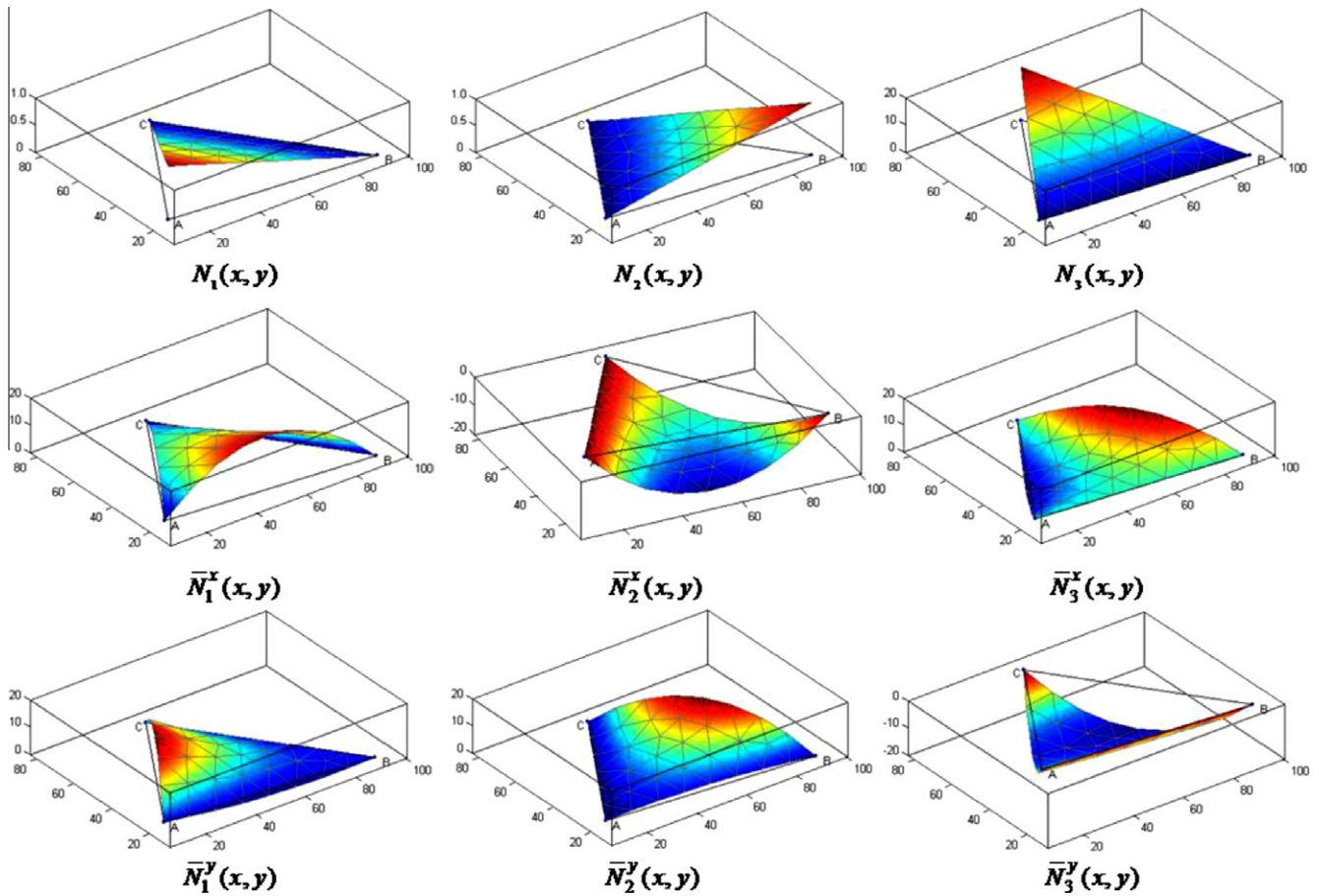


Fig. 3. Shape functions of the high order triangle element.

The element stiffness matrix of each bond is obtained as

$$\mathbf{K}^b = \frac{\partial^2 \Pi}{\partial u_i \partial u_j} = \left[ \frac{\partial^2 \Pi_b}{\partial u_i \partial u_j} \right] = (\mathbf{TB})^T \mathbf{K}_{\text{bond}} \mathbf{TB} \quad (8)$$

### 3. High order LSM

As shown in Fig. 1b, the model is composed of two types of bonds; the type-I bond belongs to one triangular element, and the type-II bond belongs to two triangular elements. The type-II

bond can also be subdivided into two type-I bonds (see Fig. 1b). To build a high order LSM, additional DOFs  $\hat{\mathbf{u}}$  are introduced to the particles, and they are linked by high order springs (see Fig. 2a). The stiffness matrices of the high order spring can be written as

$$\begin{pmatrix} \mathbf{f} \\ \hat{\mathbf{f}} \end{pmatrix} = \begin{bmatrix} \mathbf{K}^{uu} & \mathbf{K}^{u\hat{u}} \\ \mathbf{K}^{\hat{u}u} & \mathbf{K}^{\hat{u}\hat{u}} \end{bmatrix} \begin{pmatrix} \mathbf{u} \\ \hat{\mathbf{u}} \end{pmatrix} \quad (9)$$

where  $\mathbf{f}$  is the particle force,  $\hat{\mathbf{f}}$  is the general particle force,  $\mathbf{u}$  is the particle displacement,  $\hat{\mathbf{u}} = (\varepsilon_{xx}, \varepsilon_{yy})^T$  is the general DOFs which can

be viewed as stain components of the particle,  $\mathbf{K}^{uu}$  is the linear stiffness matrix and  $\mathbf{K}^{uu}$ ,  $\mathbf{K}^{uu}$  and  $\mathbf{K}^{uu}$  are the high order stiffness matrices.

Here, the PUM approximation formulation provided in Zhao et al. (2010) will be adopted to describe the local strain of the triangle element (see Fig. 2a). The displacement function is given as

$$u(x, y) = \sum_{i=1}^3 N_i \cdot u_i + \sum_{i=1}^3 N_i \cdot (x - x_i) \varepsilon_{xx}^i = \sum_{i=1}^3 N_i \cdot u_i + \sum_{i=1}^3 \bar{N}_i^x \cdot \varepsilon_{xx}^i \quad (10)$$

$$v(x, y) = \sum_{i=1}^3 N_i \cdot v_i + \sum_{i=1}^3 N_i \cdot (y - y_i) \varepsilon_{yy}^i = \sum_{i=1}^3 N_i \cdot v_i + \sum_{i=1}^3 \bar{N}_i^y \cdot \varepsilon_{yy}^i \quad (11)$$

where  $N_i$ ,  $\bar{N}_i^x$  and  $\bar{N}_i^y$  are the element shape functions associated with the particle  $i$  (see Fig. 3),  $x_i$  and  $y_i$  are the positions of the particles. The strain interpolation matrix to evaluation of the strain of the triangle element by particle displacements (the standard DOFs) can be written as

$$\mathbf{B} = [\mathbf{B}_1, \mathbf{B}_2, \mathbf{B}_3] \quad (12)$$

where  $\mathbf{B}_i$  is the sub matrix of  $i$ th particle:

$$\mathbf{B}_i = \begin{bmatrix} N_{i,x} & 0 \\ 0 & N_{i,y} \\ \frac{1}{2} N_{i,y} & \frac{1}{2} N_{i,x} \end{bmatrix} \quad (13)$$

The associated displacement vector of the particles is

$$\mathbf{u} = [u_1, v_1, u_2, v_2, u_3, v_3]^T \quad (14)$$

where  $N_i$  is the element shape function associated with the particle  $i$ .

The strain interpolation matrix  $\hat{\mathbf{B}}$  to evaluation of the strain inside the triangle element caused by the general DOFs  $\hat{\mathbf{u}}$  gives

$$\hat{\mathbf{B}} = [\hat{\mathbf{B}}_1, \hat{\mathbf{B}}_2, \hat{\mathbf{B}}_3] \quad (15)$$

where  $\hat{\mathbf{B}}_i$  is the sub matrix of  $i$ th particle:

$$\hat{\mathbf{B}}_i = \begin{bmatrix} N_{i,x}(x - x_i) + N_i & 0 \\ 0 & N_{i,y}(y - y_i) + N_i \\ \frac{1}{2} N_{i,y}(x - x_i) & \frac{1}{2} N_{i,x}(y - y_i) \end{bmatrix} \quad (16)$$

The associated general DOFs vector is

$$\hat{\mathbf{u}} = [\varepsilon_{xx}^1, \varepsilon_{yy}^1, \varepsilon_{xx}^2, \varepsilon_{yy}^2, \varepsilon_{xx}^3, \varepsilon_{yy}^3]^T \quad (17)$$

Based on the onion concept, the high order spring is divided into a number of  $N$  sub springs with same stiffness parameters (see Fig. 2b). The local stiffness matrix of each sub spring is given as

$$\mathbf{K}_{\text{bond}}^i = \frac{1}{N} \begin{bmatrix} k_n & 0 \\ 0 & k_s \end{bmatrix} \quad (18)$$

The local deformation of the  $i$ th sub spring is obtained as

$$\bar{\mathbf{u}}_i = \mathbf{T}\mathbf{s} = \mathbf{T}(\mathbf{s}^1 + \mathbf{s}^2) = \mathbf{T}(\mathbf{B}\mathbf{u} + \hat{\mathbf{B}}\hat{\mathbf{u}}) = \mathbf{T}\mathbf{B}\mathbf{u} + \mathbf{T}\hat{\mathbf{B}}\hat{\mathbf{u}} = \bar{\mathbf{u}}_i^1 + \bar{\mathbf{u}}_i^2 \quad (19)$$

Then, the strain energy stored in the bond can be written as

$$\begin{aligned} \Pi_b &= \frac{1}{2N} \sum_{i=1}^N \bar{\mathbf{u}}_i \mathbf{K}_{\text{bond}} \bar{\mathbf{u}}_i^T = \frac{1}{2N} \sum_{i=1}^N \bar{\mathbf{u}}_i^1 \mathbf{K}_{\text{bond}} \bar{\mathbf{u}}_i^{1T} + \bar{\mathbf{u}}_i^2 \mathbf{K}_{\text{bond}} \bar{\mathbf{u}}_i^{2T} \\ &\quad + \bar{\mathbf{u}}_i^1 \mathbf{K}_{\text{bond}} \bar{\mathbf{u}}_i^{2T} + \bar{\mathbf{u}}_i^2 \mathbf{K}_{\text{bond}} \bar{\mathbf{u}}_i^{1T} \end{aligned} \quad (20)$$

According to the energy minimisation principle, the stiffness matrices of the bond in Eq. (9) are obtained as

$$\mathbf{K}^{uu} = \left[ \frac{\partial^2 \Pi_b}{\partial \mathbf{u} \partial \mathbf{u}} \right] = \sum_{i=1}^N \frac{1}{N} (\mathbf{T}\mathbf{B})^T \mathbf{K}_{\text{bond}} \mathbf{T}\mathbf{B} = (\mathbf{T}\mathbf{B})^T \mathbf{K}_{\text{bond}} \mathbf{T}\mathbf{B} \quad (21)$$

$$\mathbf{K}^{\hat{u}\hat{u}} = \left[ \frac{\partial^2 \Pi_b}{\partial \hat{\mathbf{u}} \partial \hat{\mathbf{u}}} \right] = \sum_{i=1}^N \frac{1}{N} (\mathbf{T}\hat{\mathbf{B}})^T \mathbf{K}_{\text{bond}} \mathbf{T}\hat{\mathbf{B}} \quad (22)$$

$$\mathbf{K}^{\hat{u}u} = \left[ \frac{\partial^2 \Pi_b}{\partial \hat{\mathbf{u}} \partial \mathbf{u}} \right] = \sum_{i=1}^N \frac{1}{N} (\mathbf{T}\mathbf{B})^T \mathbf{K}_{\text{bond}} \mathbf{T}\hat{\mathbf{B}} \quad (23)$$

$$\mathbf{K}^{u\hat{u}} = \left[ \frac{\partial^2 \Pi_b}{\partial \mathbf{u} \partial \hat{\mathbf{u}}} \right] = \sum_{i=1}^N \frac{1}{N} (\mathbf{T}\hat{\mathbf{B}})^T \mathbf{K}_{\text{bond}} \mathbf{T}\mathbf{B} \quad (24)$$

For the linear stiffness matrix, no integration is required because the strain is constant for all sub springs. Because the higher order local strain varies depending on the centre position of the sub spring, a summarisation operation is required for high order stiffness matrices. Now, the global stiffness matrix of the high order LSM can be assembled bond by using Eqs. (21)–(24). The boundary conditions specified by displacement or force is treated as the same method as in the standard FEM.

#### 4. Spring parameters

The relationship between the spring parameters ( $k_n$  and  $k_s$ ) and the macro elastic constants, i.e., Young's modulus  $E$  and Poisson's ratio  $\nu$ , is given follows (Zhao, 2010; Zhao et al., 2011):

$$\begin{aligned} k_n &= \frac{2E}{\alpha^{2D}(1-\nu)} \\ k_s &= \frac{2(1-3\nu)E}{\alpha^{2D}(1-\nu^2)} \end{aligned} \quad (25)$$

for the plane-stress problems and

$$\begin{aligned} k_n &= \frac{2E}{\alpha^{2D}(1+\nu)(1-2\nu)} \\ k_s &= \frac{2(1-4\nu)E}{\alpha^{2D}(1+\nu)(1-2\nu)} \end{aligned} \quad (26)$$

for the plane-strain problems. Given the geometry data of the lattice spring model,  $\alpha^{2D}$  is estimated through:

$$\alpha^{2D} = \frac{\sum_{i=1}^{N_b} l_i^2}{A\Delta} \quad (27)$$

where  $l_i$  is the original length of the  $i$ th bond,  $N_b$  is the number of springs,  $A$  is the total area of the model and  $\Delta$  is the unit length to keep consistence for 2D and 3D cases (Zhao, 2010). Details of the derivation of these equations are presented in Appendix B. By inspection of Eqs. (25) and (26), it appears that the proposed model still faces a theoretical limitation, i.e., the shear stiffness will become negative when Poisson's ratios are greater than 1/3 (plane-stress) or 1/4 (plane-strain). The negative stiffness of shear spring seems non-physical, but the negative stiffness can have a physical explanation at the molecular level. This is discussed in Appendix

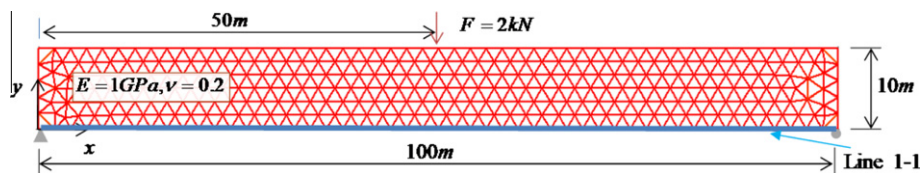


Fig. 4. The geometry and boundary conditions for the beam bending problem.

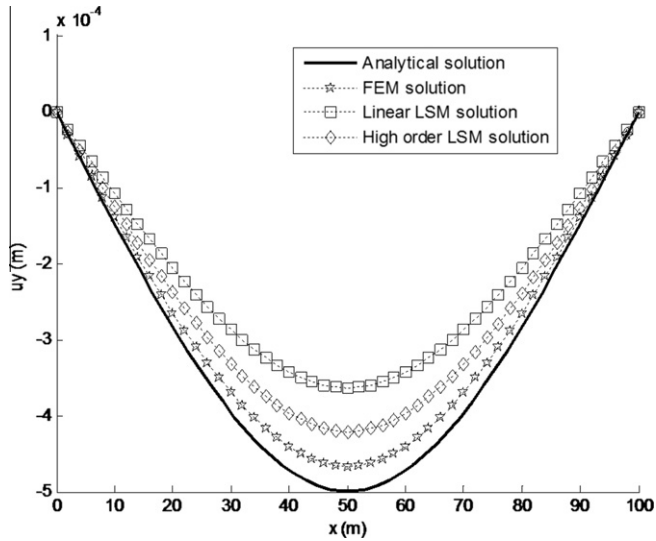


Fig. 5. The displacement results predicted by high order LSM, linear LSM and FEM for the beam bending problem.

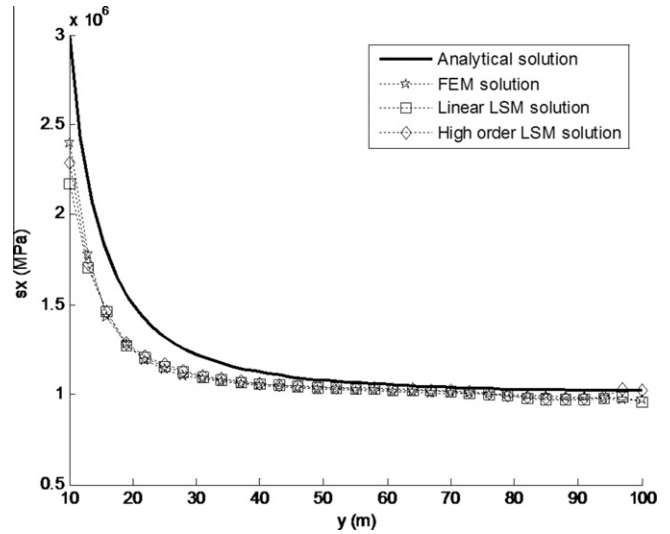


Fig. 7. The stress results predicted by high order LSM, linear LSM and FEM for the circle hole problem.

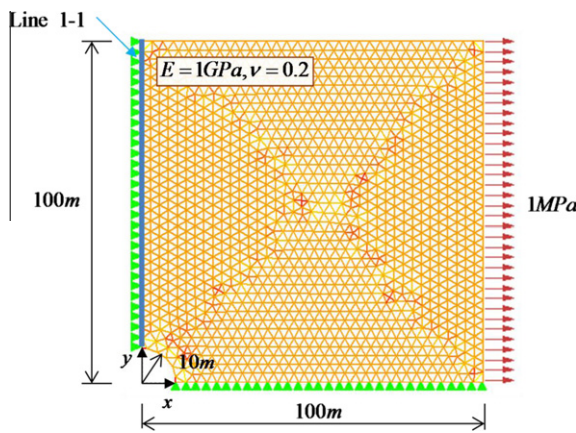


Fig. 6. The geometry and boundary conditions for the circular hole plate under tensile problem.

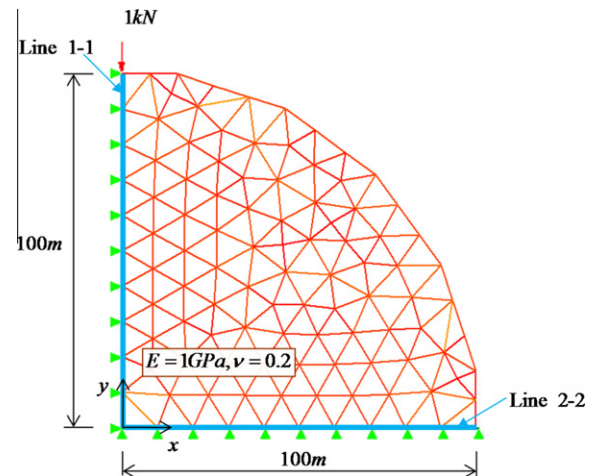


Fig. 8. The geometry and boundary conditions for the Brazilian disc problem.

C. Moreover, this limitation is practically not true for DLSM, as the shear spring of negative stiffness can be added in the model, and the final algebraic equation is still solvable. Details can be found in reports by Zhao (2010) and Zhao et al. (2011).

5. Verification

5.1. Beam bending problem

The geometry and boundary conditions of the problem are described in Fig. 4. The bottom-right corner is fixed in the y-direction, and bottom-left corner is fixed in both the x- and y- directions. A force of 2 kN is applied at middle point the beam. The elastic constants of the beam, i.e., Young’s modulus and Poisson’s ratio, are 1GPa and 0.20, respectively. The LSM and FEM are based on the same triangular mesh (see Fig. 4). Fig. 5 shows the displacement of bottom line of the beam predicted by the high order LSM, linear LSM, FEM and the corresponding analytical solution. The analytical solution is

$$u_y(x) = \begin{cases} \frac{Fx(4x^2-3L^2)}{48EI}, & 0 \leq x < \frac{L}{2} \\ \frac{F(L-x)(4(L-x)^2-3L^2)}{48EI}, & \frac{L}{2} \leq x < L \end{cases} \quad (28)$$

where  $u_y$  is the displacement of the beam in y direction,  $F$  is the applied force,  $L$  is the length of the beam,  $E$  is the elastic modulus of the beam, and  $I$  is the moment of inertia which equals to  $bh^3/12$  where  $b$  and  $h$  are width (1 m) and height of the beam section. The FEM predicted the best result, and the linear LSM produced the worst one. Compared with the linear LSM, the developed high order LSM predicted a much better result. This demonstrates the benefit of introducing the high order spring in LSM.

5.2. Circle hole plate subjected to tensile stress

In this section, a classical problem in elasticity is solved. Fig. 6 shows the geometry, the loading condition, and the lattice model used in this section. The radius of the hole is 10 m, and the width of the plane is 200 m. To save computation time, only the 1/4 model is used (see Fig. 6). The left and bottom surfaces are fixed in the x- and y- directions, respectively. A tensile stress of 1 MPa is applied on the right surface. The elastic constants are  $E = 1$  GPa and  $\nu = 0.2$ . The spring parameters are obtained according to Eq. (23). The modelling results of different models are shown in Fig. 7. Again, a good match between the results by analytical solution and the solutions by FEM, linear LSM and high order LSM is observed. The analytical solution of  $s_x$  along line 1–1 can be given as

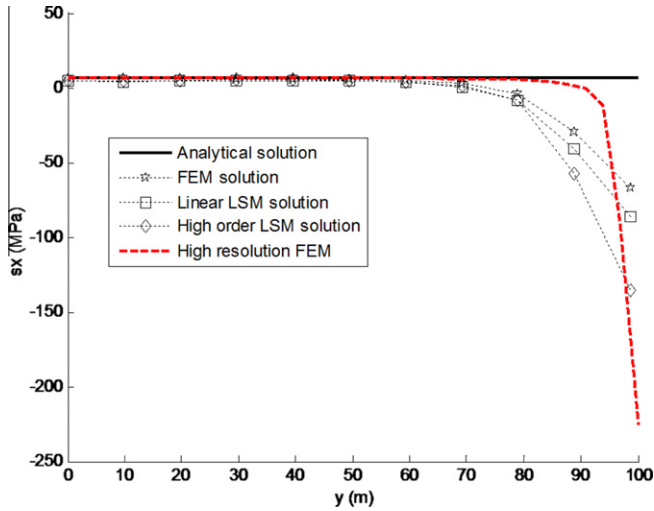


Fig. 9. The stress results predicted by high order LSM, linear LSM, FEM, high resolution FEM, and the analytical solution for the Brazilian disc problem along Line 1-1.

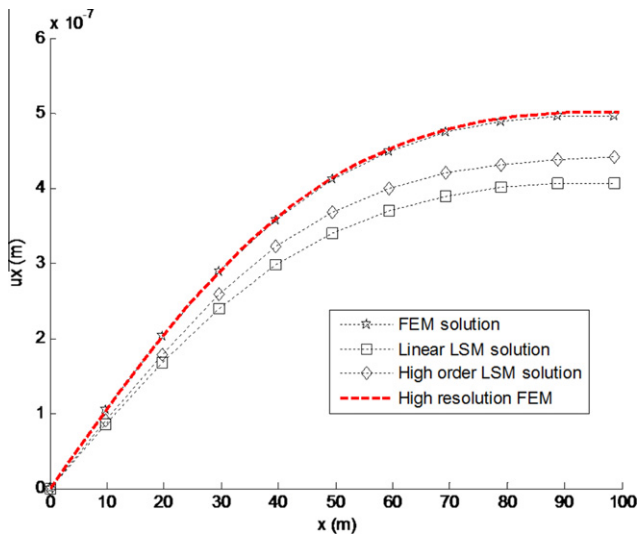


Fig. 10. The displacement results predicted by high order LSM, linear LSM and FEM for the Brazilian disc problem along Line 2-2.

$$s_x(y) = p \left( 1 + \frac{2r^2}{y^2} \right) \quad (29)$$

where  $p$  is the applied tensile stress, and  $r$  is radius of the hole. For this example, the solutions between the different methods are similar. However, compared with linear LSM, the high order LSM still gives better results (see Fig. 7).

### 5.3. Brazilian disc

In this section, the Brazilian disc problem is analysed. As shown in Fig. 8, the 1/4 model is used. The left and bottom surfaces are fixed in the  $x$ - and  $y$ - directions, respectively. A point force of 1 kN is applied at the top of the disc (see Fig. 8). The elastic constants are  $E = 1\text{GPa}$  and  $\nu = 0.2$ . Two section lines, Line 1-1 and Line 2-2, are used to record the simulation results (see Fig. 8). In DEM, stress of the model is calculated using following equation (Potyondy and Cundall, 2004).

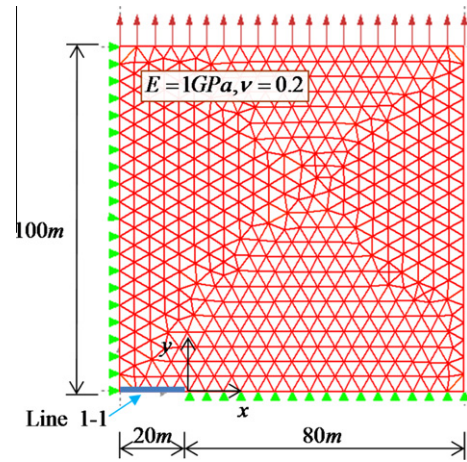


Fig. 11. The geometry and boundary conditions for the centre cracked plate under tensile loading.

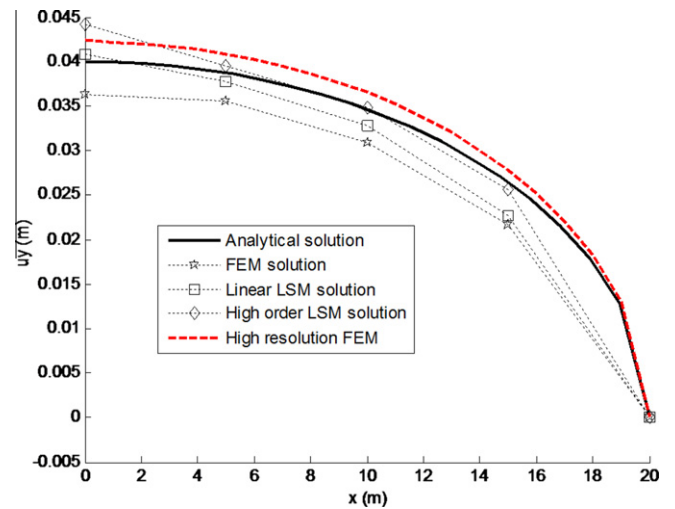


Fig. 12. The crack opening predicted by the high order LSM, linear LSM, FEM, analytical solution and high resolution FEM for the centre cracked plate under tensile loading problem.

$$\bar{\sigma}_{ij} = - \left( \frac{1-n}{\sum_{N_p} V_{(p)}} \right) \sum_{N_p} \sum_{N_c} |x_i^{(c)} - x_i^{(p)}| n_i^{(c,p)} F_j^{(c)} \quad (30)$$

where  $N_p$  is the number of particles contained within the measurement region and the  $N_c$  is the contact of these particles,  $n$  is the porosity with the measurement region,  $V_{(p)}$  is the volume of particle ( $p$ ),  $x_i^{(c)}$  and  $x_i^{(p)}$  are the locations of a particle centroid and its contact,  $n_i^{(c,p)}$  is the normal from a particle to its contact, and  $F_j^{(c)}$  is the contact force. Details can be found in the work of Potyondy and Cundall (2004). For the LSMs, since input parameters are macro elastic parameters and the strains of particles are also available during calculation, the stresses were calculated directly using the elastic constitutive relationship. Fig. 9 shows the results of stress in the  $x$ -direction along the disc centreline (Line 1-1). This shows that the FEM, linear LSM and high order LSM are in good agreement with the analytical solution  $2P/\pi Dt$  (here,  $P$  is the applied load,  $D$  is the diameter of the disc and  $t$  is the unit thickness). Because the analytical solution did not take into account the stress singularity, one high resolution FEM model with a mesh size ten times smaller is used as the numerical reference. Compared with FEM, LSMs can

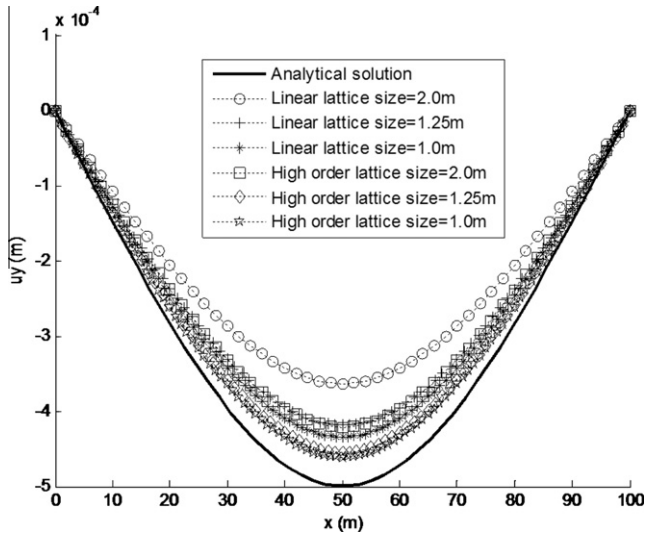


Fig. 13. The beam bending problem predicted by LSMs with different lattice sizes.

produce a better fit around the singularity point (see Fig. 9). This means that the LSMs may be more suitable for singularity problems. Results of the displacement in the  $x$ -direction along the section Line 2–2 are also presented in Fig. 10. It can be seen that the high order LSM produced better results than the linear LSM.

5.4. Centre cracked plate under tensile loading

In the previous example, the LSMs provided better results around the singularity point than the FEM. To further study whether LSM is still superior in modelling the classical singularity problem of a crack, the centre cracked plate under tensile problem is simulated in this section. Fig. 11 shows the 1/4 model of the problem. The model size is 100 m, and the half crack length is 20 m. The elastic constants are  $E = 1$  GPa and  $\nu = 0.2$ . A tensile stress of 1 MPa is applied along the top surface. The analytical solution for the opening of the crack surface in an infinite domain and the high resolution FEM solution are used as references. The analytical solution is given as

$$u_y = \frac{2ap}{E} \sqrt{1 - \left(\frac{x}{a}\right)^2} \tag{31}$$

where  $a$  is the crack length,  $E$  is the elastic modulus,  $p$  is the applied stress. The modelling results of different models are shown in Fig. 12. The results show that LSMs work better than FEM with the same mesh resolution. Compared with the results of FEM, the predicted crack openings of LSMs are closer to the analytical and high resolution FEM results (see Fig. 12). Combining the results of the previous sections, it may be preliminarily concluded that LSMs are more suitable for modelling singularity problems than FEM. Researchers of LSMs are always declaring that LSMs are superior to FEM for modelling fracturing problem due to the discrete nature

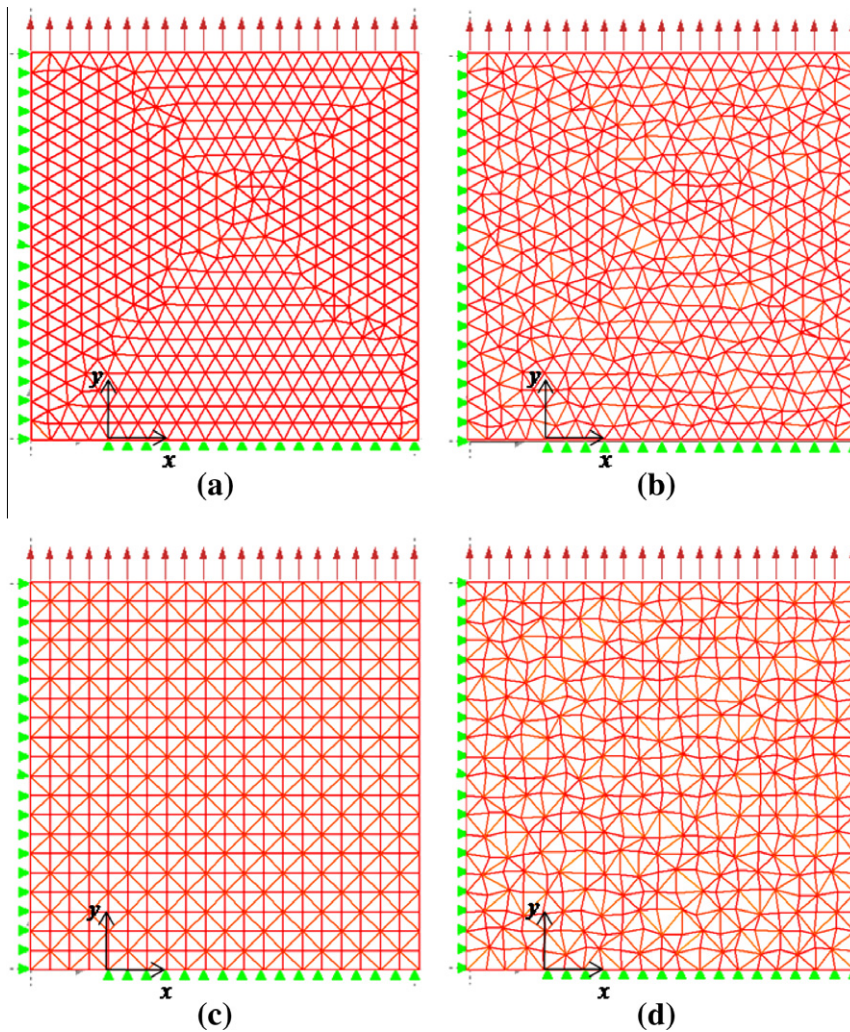


Fig. 14. Different lattice structures for the high order LSM.

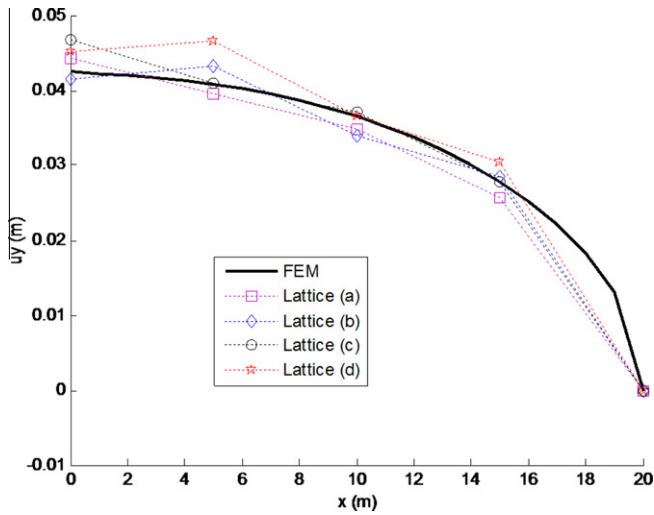


Fig. 15. The results of high order LSM on centre cracked plate under tensile loading problem with different lattice structures.

Table 1  
Layout parameters of the sub springs.

Layout	Sub spring I			Sub spring II		
	$w_1$	$w_2$	$w_3$	$w_1$	$w_2$	$w_3$
<i>a</i>	0.50	0.50	0.00	0.50	0.50	0.00
<i>b</i>	0.75	0.25	0.00	0.25	0.75	0.00
<i>c</i>	0.40	0.40	0.20	0.40	0.40	0.20
<i>d</i>	0.55	0.30	0.15	0.30	0.55	0.15

of LSMs. From the result of this section, the LSM representation of a solid can produce better results for the singularity area, which is additional strong evidence of the advantage of LSM over FEM for modelling fracturing problems.

## 6. Discussion

### 6.1. Lattice size

The convergence of the high order LSM is studied in this section. The beam bending problem in Section 5.1 is solved using models with different lattice sizes. The results are displayed in Fig. 13, which show that by decreasing the lattice size, both linear LSM and high order LSM are close to the analytical solution. Due to the computational limitation of our current code, only a model with the smallest lattice size of 1.0 m can be studied. It is believed

that a better solution can be obtained from using a finer mesh by decreasing the lattice size. As shown in Fig. 13, high order LSM with lattice size of 2 m gives displacement solution between linear LSMs whose lattice sizes are 1.25 m and 1.0 m. The corresponding computational times are 10 s, 12 s and 18 s, respectively. To have a mathematic proof, assume there is a square domain with size of  $H$ , which was meshed into regular triangle lattice model with lattice size of  $l$ . The total DOFs for linear LSM and high order LSM will be  $2 \times (H/l)^2$  and  $4 \times (H/l)^2$ . If a linear LSM with lattice size of 1.00/2.00 or 1.25/2.00 times as that of a high order LSM will produce an equivalent prescient solution, the total DOFs for the linear LSM will be 2.00 or 1.28 times as that for the high order LSM. Therefore, the high order LSM is more computational effective. Moreover, the high order LSM can improve the solution without re-meshing the model. The singularity enrichment of XFEM can also be incorporated to LSM by introducing special general DOFs, which will bring the advantage of XFEM into LSMs.

### 6.2. Lattice structure

The influence of lattice structure is studied by comparing the results of four different lattice structures on the crack problem in Section 5.4. As shown in Fig. 14, structure *a* is made of particles with a slight irregular distribution, structure *c* consists of particles with a regular distribution, and structures *b* and *d* are obtained by randomly moving the particles in structures *a* and *c*, respectively. The results for this study are summarised in Fig. 15, which shows that the regular disturbed lattice structures (*b*, *d*) will produce disturbed results while the random lattice structure will produce stable results. This means that the lattice model is mesh dependent. In other words, the lattice model can reflect the microstructure information of the model, which is important for fracture simulations. The proposed high order LSM adopts the PUM technique, and inherits the discrete nature of LSM as well. This feature may lead it to be a suitable method for fracture simulation of materials. For example, the singularity of crack tip can be captured by using the enrichment technique in XFEM, while the cracked surface (discontinuity) be represented by springs between particles.

### 6.3. Sub spring layout

The influence of the layout method of sub springs on the simulation results of the high order LSM is studied. The centre point of the sub spring is calculated from

$$x_c^{sub} = \sum_{i=1}^3 x_i w_i, y_c^{sub} = \sum_{i=1}^3 y_i w_i \quad (32)$$

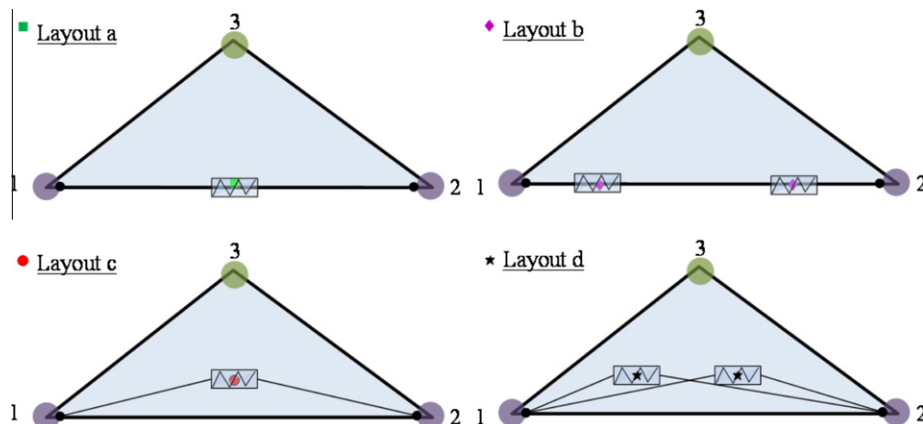


Fig. 16. Different layouts of sub springs.

where  $x_i$  and  $y_i$  are the position of the nodes of the linked FEM element, and  $w_i$  is the layout parameter. In this section, two sub springs are used. The layout parameters for different layouts are listed in Table 1. The corresponding configuration graphics are shown in Fig. 16. The beam bending problem in Section 5.1 and the crack problem in Section 5.4 are used to study the influence of sub spring layout on the simulation results. The modelling results on the beam bending problem are shown in Fig. 17a. It can be seen that layout c predicts the best solution while layout a will produce the same solution as the linear LSM. From Fig. 17b, it was found that layout c will result in unstable results for the cracking problem. Therefore, from observing the simulation results in Fig. 17, layout d is the recommended sub spring layout.

6.4. Fracture simulation

In this section, one fracture simulation will be performed using the developed high order LSM. The geometry and the loading setup for the three bending beams test are shown in Fig. 18. The controlled displacement on the top begins with 0.0 mm and increase gradually to 0.5 mm during the test (100 steps in total, 0.005 mm

per step). The elastic constants of the material are  $E = 10^3$  MPa and  $\nu = 0.2$ . The tensile strength is given as 1 MPa. Again, the spring parameters are obtained according to Eq. (23). Because the purpose of this example is to demonstrate the easy feature of the LSM for fracture simulation, we only consider the tensile failure of bond, which occurs when

$$u_n > \delta_t^* \tag{33}$$

where  $u_n$  is the normal deformation of the bond, and  $\delta_t^*$  is the limit value of the bond's stretching. During the simulation, whenever a bond fails, it is deleted from the calculation procedure. In the proposed LSM, different lattice structures can be used, and length of bonds are not constant. Therefore, the mean length of the bonds is used to calculate the limit value  $\delta_t^*$  as  $l^* \sigma_t / E$  (here,  $l^*$  is the mean length of the bonds,  $\sigma_t$  is the tensile strength of the material and  $E$  is the elastic modulus). For the current simulation, the mean bond length (lattice) is 8 mm. For comparison purposes, the FEM model based on the element deletion method and linear LSM are also used to simulate this problem. The predicted loading curves from different methods are shown in Fig. 19. The results show that the linear LSM predicted stiffer results when compared with the FEM and the high order LSM. The final failure configurations for different models are shown in Fig. 20. For LSMs, the bond, in which failure occurs, is marked by double red lines around the centre of the bond. As shown in Fig. 18, a “V” type fracture surface is produced by the CDM FEM, while “I” type crack is given by the high order LSM. With regard to

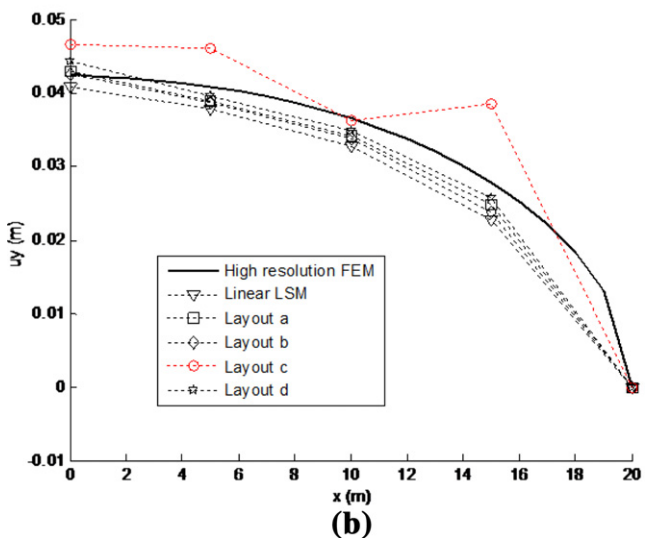
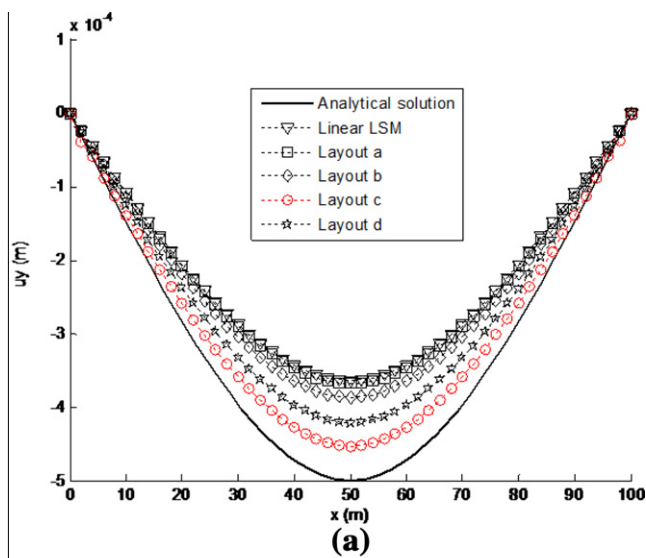


Fig. 17. Influence of the sub spring layout on solution of the high order LSM (a) the beam bending problem, (b) the crack problem.

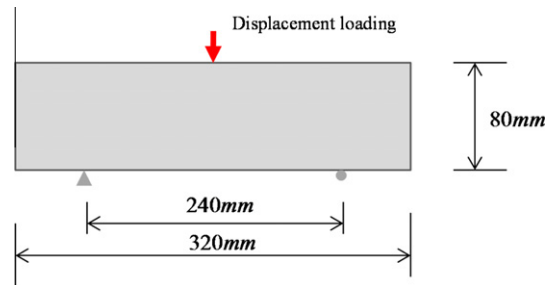


Fig. 18. The three-point beam bending tensile test.

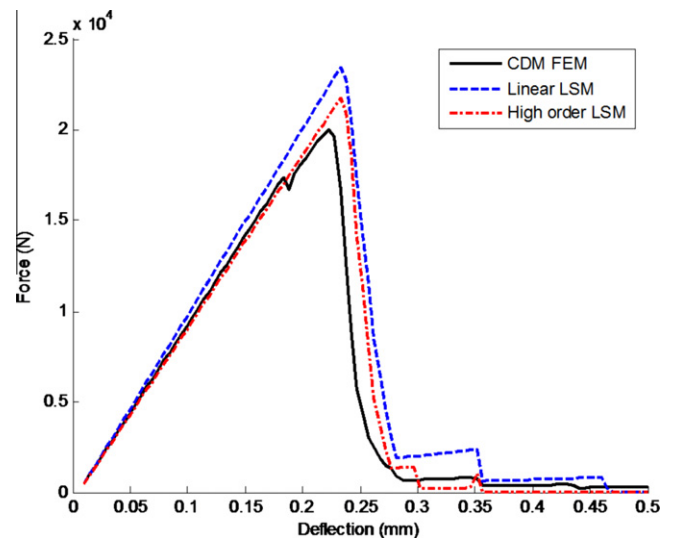


Fig. 19. The deflection loading curves simulated by high order LSM, linear LSM and FEM for the beam bending test.

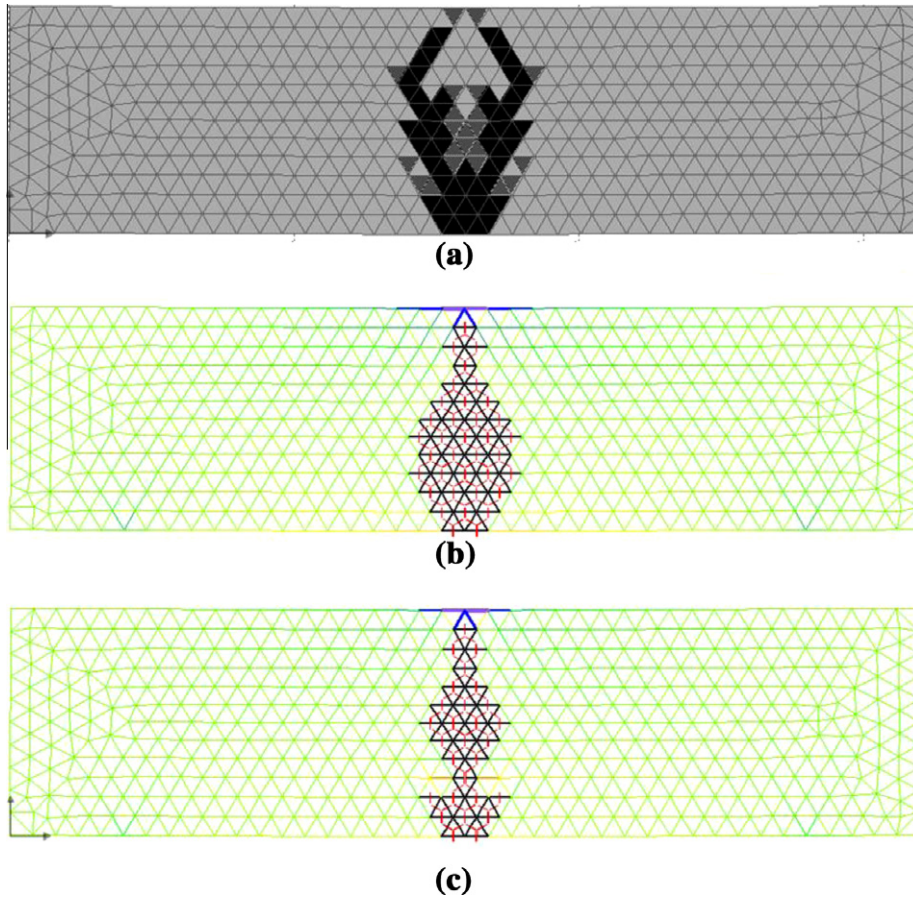


Fig. 20. Fracture patterns predicted by different methods (a) FEM, (b) linear LSM and (c) high order LSM.

the crack patterns obtained, the simulation of the high order LSM gives a realistic description of the fracture pattern observed in experimental tests. This example only shows the ability of the high order LSM on fracture simulation. More sophisticated bond fracture criteria and crack tip enrichment functions can be implemented in the model for more realistic modelling of fracture processes.

## 7. Conclusions

This paper presents a high order LSM, in which general DOFs are introduced to describe the spring deformation based on the local strain technique provided by DLSM. The formulations for high order springs are derived based on the energy minimisation principle. The high order LSM is more capable of capturing the mechanical deformation than that of linear LSM. It is also found that the high order LSM can provide better results for singularity problems. The influence of lattice size, lattice structure and layout of sub-springs are studied. The recommended sub spring layout is presented. One fracture problem is simulated by the proposed high order LSM, and when the results are compared with the FEM with the element deletion technique, the proposed model provides better results. The paper focused on development of a high order LSM to describe the basic linear elastic behaviour of material. To model more realistic constitutive behaviour of materials, advanced constitutive laws, e.g., the visco-elastic model proposed by O'Brien (2008), cohesive spring constitutive law by Kazerani et al. (2010), and the plastic constitutive model for LSM by Buxton et al. (2001), can be further implemented.

## Appendix A

### A.1. Proof of the discrete nature of Eq. (1)

In this appendix, Eq. (1) for evaluating the deformation of bond springs in DLSM is derived and its discrete nature will be apparent. First, consider a cubic unit containing a bond connecting two particles ( $P_1$  and  $P_2$ ) as shown in Fig. A1.

The complete 1st order displacement function of the cubic is

$$\begin{pmatrix} u_x \\ u_y \end{pmatrix} = \begin{pmatrix} a_0 & a_1 & a_2 \\ b_0 & b_1 & b_2 \end{pmatrix} \begin{pmatrix} 1 \\ x \\ y \end{pmatrix} \quad (\text{A.1})$$

where  $a_i$  and  $b_i$  are coefficients of the displacement function.

Assuming the centre of the block at  $(x_c, y_c)$ , its displacement is represented by

$$\begin{pmatrix} u_{cx} \\ u_{cy} \end{pmatrix} = \begin{pmatrix} a_0 & a_1 & a_2 \\ b_0 & b_1 & b_2 \end{pmatrix} \begin{pmatrix} 1 \\ x_c \\ y_c \end{pmatrix} \quad (\text{A.2})$$

Subtracting (A.2) from (A.1) gives

$$\begin{pmatrix} u_x \\ u_y \end{pmatrix} - \begin{pmatrix} u_{cx} \\ u_{cy} \end{pmatrix} = \begin{pmatrix} a_0 & a_1 & a_2 \\ b_0 & b_1 & b_2 \end{pmatrix} \begin{pmatrix} 1 \\ x \\ y \end{pmatrix} - \begin{pmatrix} a_0 & a_1 & a_2 \\ b_0 & b_1 & b_2 \end{pmatrix} \begin{pmatrix} 1 \\ x_c \\ y_c \end{pmatrix} \quad (\text{A.3})$$

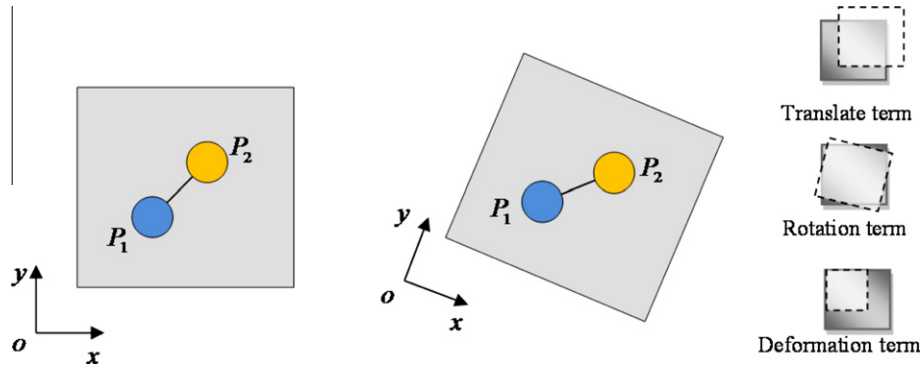


Fig. A1. Illustration of the deformation of a cubic unit with a bond connecting two particles.

Eq. (A.3) can be further written as

$$\begin{pmatrix} u_x \\ u_y \end{pmatrix} = \begin{pmatrix} u_{cx} \\ u_{cy} \end{pmatrix} + \begin{pmatrix} a_1 & 0 \\ 0 & b_2 \end{pmatrix} \begin{pmatrix} x - x_c \\ y - y_c \end{pmatrix} + \begin{pmatrix} 0 & a_2 \\ b_1 & 0 \end{pmatrix} \begin{pmatrix} x - x_c \\ y - y_c \end{pmatrix} \quad (\text{A.4})$$

From (A.4), we have

$$\begin{aligned} \varepsilon_{xx} &= \frac{\partial u_x}{\partial x} = a_1 \\ \varepsilon_{yy} &= \frac{\partial u_y}{\partial y} = b_2 \end{aligned}$$

$$\varepsilon_{xy} = \frac{1}{2} \left( \frac{\partial u_y}{\partial x} + \frac{\partial u_x}{\partial y} \right) = \frac{1}{2} (b_1 + a_2)$$

$$\omega = \frac{1}{2} \left( \frac{\partial u_y}{\partial x} - \frac{\partial u_x}{\partial y} \right) = \frac{1}{2} (b_1 - a_2)$$

where  $\varepsilon_{ij}$  are the strain components of the cubic and  $\omega$  is the rotation of the cubic.

Using the above relations, Eq. (A.4) can be transformed into

$$\begin{pmatrix} u_x \\ u_y \end{pmatrix} = [D_0] \begin{pmatrix} u_{cx} \\ u_{cy} \end{pmatrix} + [D_1](\omega) + [D_2] \begin{pmatrix} \varepsilon_{xx} \\ \varepsilon_{yy} \end{pmatrix} + [D_3](\varepsilon_{xy}) \quad (\text{A.5})$$

where

$$[D_0] = \begin{pmatrix} 1 & 0 \\ 0 & 1 \end{pmatrix}$$

$$[D_1] = \begin{pmatrix} -(y - y_c) \\ x - x_c \end{pmatrix}$$

$$[D_2] = \begin{pmatrix} x - x_c & 0 \\ 0 & y - y_c \end{pmatrix}$$

$$[D_3] = \begin{pmatrix} y - y_c \\ x - x_c \end{pmatrix}$$

Denoting the coordinates of the two particles in the cubic as  $(x_1, y_1)$  and  $(x_2, y_2)$  and their displacement as  $(u_1, v_1)$  and  $(u_2, v_2)$ , the relative displacement vector between the two particles is

$$\begin{pmatrix} u_{12x} \\ u_{12y} \end{pmatrix} = \begin{pmatrix} u_{2x} - u_{1x} \\ u_{2y} - u_{1y} \end{pmatrix} \quad (\text{A.6})$$

and the normal unit vector is

$$\begin{pmatrix} n_x \\ n_y \end{pmatrix} = \begin{pmatrix} \frac{x_2 - x_1}{l} \\ \frac{y_2 - y_1}{l} \end{pmatrix} \quad (\text{A.7})$$

where  $l$  is the length of the bond. The relative normal displacement vector is defined as

$$\begin{pmatrix} u_{12x}^n \\ u_{12y}^n \end{pmatrix} = \begin{pmatrix} (u_{12x})^T (n_x) \\ (u_{12y})^T (n_y) \end{pmatrix} \begin{pmatrix} n_x \\ n_y \end{pmatrix} \quad (\text{A.8})$$

By vector operation, the relative shear displacement vector is obtained as

$$\begin{pmatrix} u_{12x}^s \\ u_{12y}^s \end{pmatrix} = \begin{pmatrix} u_{12x} \\ u_{12y} \end{pmatrix} - \begin{pmatrix} u_{12x}^n \\ u_{12y}^n \end{pmatrix} = \begin{pmatrix} u_{12x} \\ u_{12y} \end{pmatrix} - \left( \begin{pmatrix} u_{12x} \\ u_{12y} \end{pmatrix}^T \begin{pmatrix} n_x \\ n_y \end{pmatrix} \right) \begin{pmatrix} n_x \\ n_y \end{pmatrix} \quad (\text{A.9})$$

Now, applying Equation (A.5), the relative displacement vector can be represented as

$$\begin{pmatrix} u_{2x} - u_{1x} \\ u_{2y} - u_{1y} \end{pmatrix} = \underbrace{\begin{pmatrix} x_2 - x_1 & 0 \\ 0 & y_2 - y_1 \end{pmatrix} \begin{pmatrix} \varepsilon_{xx} \\ \varepsilon_{yy} \end{pmatrix} + \varepsilon_{xy} \begin{pmatrix} y_2 - y_1 \\ x_2 - x_1 \end{pmatrix}}_{\text{strain related term}} + \underbrace{\omega \begin{pmatrix} -(y_2 - y_1) \\ x_2 - x_1 \end{pmatrix}}_{\text{rotation related term}} \quad (\text{A.10})$$

With the above equation, it is straightforward to show that the relative normal displacement vector is dependant only on the strain related term because of the following equivalence

$$\begin{pmatrix} -(y_2 - y_1) \\ x_2 - x_1 \end{pmatrix}^T \begin{pmatrix} x_2 - x_1 \\ y_2 - y_1 \end{pmatrix} = 0$$

However, for the relative shear displacement vector, if we directly substitute (A.10) into (A.9), the related rotation term will not vanish. It is known that the rigid rotation of the cube should not produce strain energy. Therefore, in DLSM, the rotation related term is removed from the calculation of the relative shear displacement vector, namely, the relative displacement vector in (A.9) is not calculated anymore by using (A.10) or (A.6) but by the following

$$\begin{aligned} \begin{pmatrix} \hat{u}_{12x} \\ \hat{u}_{12y} \end{pmatrix} &= \begin{pmatrix} x_2 - x_1 & 0 \\ 0 & y_2 - y_1 \end{pmatrix} \begin{pmatrix} \varepsilon_{xx} \\ \varepsilon_{yy} \end{pmatrix} + \varepsilon_{xy} \begin{pmatrix} y_2 - y_1 \\ x_2 - x_1 \end{pmatrix} \\ &= \begin{pmatrix} \varepsilon_{xx} & \varepsilon_{xy} \\ \varepsilon_{xy} & \varepsilon_{yy} \end{pmatrix} \begin{pmatrix} x_2 - x_1 \\ y_2 - y_1 \end{pmatrix} \end{aligned} \quad (\text{A.11})$$

Writing (A.11) in the vector form, we get

$$\hat{\mathbf{u}}_{ij} = [\boldsymbol{\varepsilon}] \cdot \mathbf{n} \quad (\text{A.12})$$

Finally, the relative shear displacement vector, the vector form of (A.9), can be written as

$$\hat{\mathbf{u}}_{ij}^s = [\boldsymbol{\varepsilon}] \cdot \mathbf{n} - (([\boldsymbol{\varepsilon}] \cdot \mathbf{n}) \cdot \mathbf{n}) \mathbf{n} \quad (\text{A.13})$$

Then, the magnitude of shear deformation can be given as

$$\hat{u}^s = ([\boldsymbol{\varepsilon}] \cdot \mathbf{n} - (([\boldsymbol{\varepsilon}] \cdot \mathbf{n}) \cdot \mathbf{n}) \mathbf{n}) \cdot \mathbf{n}' \quad (\text{A.14})$$

where  $\mathbf{n}' = (-n_y, n_x)^T$  is the unit vector perpendicular to  $\mathbf{n}$ . In summary, the normal and shear deformation of the bond can be expressed as

$$\hat{u}^n = ([\boldsymbol{\varepsilon}] \cdot \mathbf{n}) \cdot \mathbf{n} \quad (\text{A.15})$$

$$\hat{u}^s = ([\boldsymbol{\varepsilon}] \cdot \mathbf{n}) - (([\boldsymbol{\varepsilon}] \cdot \mathbf{n}) \cdot \mathbf{n}) \mathbf{n} \quad (\text{A.16})$$

Eqs. (A.15) and (A.16) can be further rewritten as

$$\hat{u}^n = l n_x^2 \varepsilon_{xx} + l n_y^2 \varepsilon_{yy} + 2l n_x n_y \varepsilon_{xy} \quad (\text{A.17})$$

$$\hat{u}^s = -l n_x n_y \varepsilon_{xx} + l n_x n_y \varepsilon_{yy} + l (n_x^2 - n_y^2) \varepsilon_{xy} \quad (\text{A.18})$$

Using the matrix form, these equations can be expressed as  $\hat{\mathbf{u}} = \mathbf{T}\boldsymbol{\varepsilon}$ . Now, it can be seen that the Eq. (1) represents the relative particle deformation in normal and shear directions under the rotationally invariant condition.

## Appendix B

### B.1. Relationship between spring parameters and elastic constants

In this section, the relationship between spring parameters and elastic constants is derived by following the approach used in the virtual multi-dimensional internal bond model (Zhang and Ge, 2005; Zhao, 2010). The microstructure of the model is shown in Fig. B1(a). Spherical particles are distributed randomly in space. The particles are not restricted to the same size. Whenever two particles are detected in contact, they are linked together through bonds between their center points. The internal bond includes one normal spring and one shear spring for both 3D case and 2D case. Consider a deformation state  $\varepsilon_{ij}$  imposed on the cube. As the cube is represented through internal bonds, the energy stored in the continuum element is equal to the sum of energy stored in each bond. As translation operation of bonds will not influence their deformation energy, the distribution of bonds in the cube could be equivalent to a semi sphere distribution as shown in Fig. B1(b). Using the spherical coordinate system for 3D or circular coordinate for 2D as shown in Fig. B1(c), the total strain energy stored per unit volume is

$$\Pi = \frac{\sum \Pi_b}{A\Delta} = \sum \frac{l^2 (k_n \xi_i \varepsilon_{ij} \xi_j \xi_n \varepsilon_{nm} \xi_m + k_s \xi_i \varepsilon_{ij} \eta_j \xi_n \varepsilon_{nm} \eta_m)}{2A\Delta} \quad (\text{B.1})$$

where  $A$  is the area of the modelling domain,  $\Delta$  is the unit length in the third dimension,  $\xi$  is the direction vector of the bond, which is  $(n_x, n_y)$ ,  $\varepsilon_{ij}$  is the imposed strain,  $k_n$  is the normal stiffness of the bond,  $k_s$  is the shear stiffness of the bond and  $\eta$  is the unit vector perpendicular to  $\xi$ , which is  $(-n_y, n_x)$ . The stress tensor of the continuum can be obtained through the Cauchy-born rule (Tadmor et al., 1996) and the hyperelastic theory (Marsden and Hughes, 1983), and it can be written as

$$\sigma_{ij} = \frac{\partial \Pi}{\partial \varepsilon_{ij}} = \sum \frac{l^2 (k_n \xi_i \xi_j \xi_n \varepsilon_{nm} \xi_m + k_s \xi_i \eta_j \xi_n \varepsilon_{nm} \eta_m)}{A\Delta} \quad (\text{B.2})$$

The elastic modulus is expressed as

$$c_{ijnm} = \frac{\partial^2 \Pi}{\partial \varepsilon_{ij} \partial \varepsilon_{nm}} = \sum \frac{l^2 (k_n \xi_i \xi_j \xi_n \xi_m + k_s \xi_i \eta_j \xi_n \eta_m)}{A\Delta} \quad (\text{B.3})$$

When the total number of bonds is large enough, Eq. (B.1) can be written in the integral form as

$$c_{ijnm} = \frac{1}{A\Delta} \int_{l_1}^{l_2} \int_0^\pi l^2 (k_n \xi_i \xi_j \xi_n \xi_m + k_s \xi_i \eta_j \xi_n \eta_m) D(l, \beta) d\beta dl \quad (\text{B.4})$$

where  $D(l, \beta) d\beta dl$  is the number of bonds with bond length between  $(l, l + dl)$  and bond orientation between  $(\beta, \beta + d\beta)$ . For the isotropic material, the bonds distribute uniformly in each direction. Therefore, the bond distribution function  $D(l, \beta)$  is reduced to  $N(l)/\pi$  with  $N(l)dl$  being the number of bonds with length between  $(l, l + dl)$ . In numerical methods, e.g., FEM, the elastic tensor  $c_{ijnm}$  is often written in the elastic matrix form as follows:

$$\boldsymbol{\Omega} = \begin{bmatrix} C_{1111} & C_{1122} & \frac{1}{2}(C_{1112} + C_{1121}) \\ C_{2211} & C_{2222} & \frac{1}{2}(C_{2212} + C_{2221}) \\ C_{1211} & C_{1222} & \frac{1}{2}(C_{1212} + C_{1221}) \end{bmatrix} \quad (\text{B.5})$$

For the linear elastic cases, the tangent modulus is equal to the secant modulus, and Equation (B.2) can be considered as the secant modulus. Therefore, the following relationship exists:

$$\boldsymbol{\sigma} = \boldsymbol{\Omega} \cdot \boldsymbol{\varepsilon} \quad (\text{B.6})$$

where  $\boldsymbol{\sigma} = [\sigma_{11}, \sigma_{22}, \sigma_{12}]^T$  and  $\boldsymbol{\varepsilon} = [\varepsilon_{11}, \varepsilon_{22}, 2\varepsilon_{12}]^T$ . Here,  $\sigma_{ij}$  and  $\varepsilon_{ij}$  are the components of the stress and strain tensors, respectively. By integrating Eq. (B.2) and using Eq. (B.3), the corresponding elastic matrix is obtained as:

$$\boldsymbol{\Omega} = \frac{\int_{l_1}^{l_2} l^2 N(l) dl}{8A\Delta} \begin{bmatrix} 3k_n + k_s & k_n - k_s & 0 \\ & 3k_n + k_s & 0 \\ \text{symmetry} & & k_n + k_s \end{bmatrix} \quad (\text{B.7})$$

Let  $\alpha^{2D} = \int_{l_1}^{l_2} l^2 N(l) dl / A\Delta$ , then the relationship between the spring parameters ( $k_n$  and  $k_s$ ) and the macro elastic constants, i.e. Young's modulus  $E$  and Poisson's ratio  $\nu$  can be obtained from Eq. (B.7) as follows:

$$\begin{aligned} k_n &= \frac{2E}{\alpha^{2D}(1-\nu)} \\ k_s &= \frac{2(1-3\nu)E}{\alpha^{2D}(1-\nu^2)} \end{aligned} \quad (\text{B.8})$$

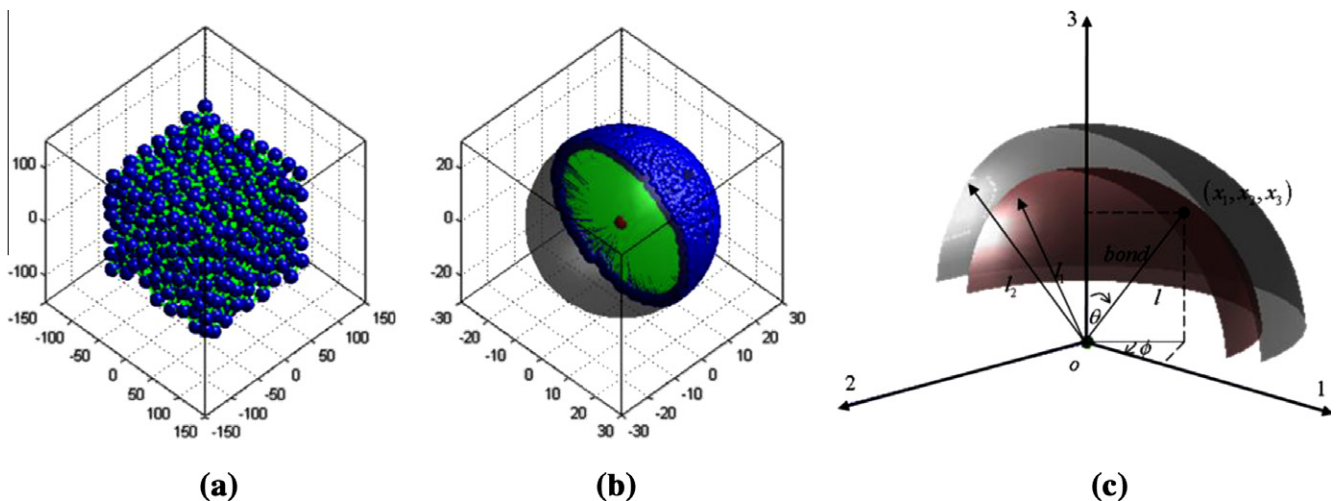


Fig. B1. Microstructure model of the RMIB model (a) particle model, (b) energy equivalent form, and (c) bond distribution under spherical coordinate system.

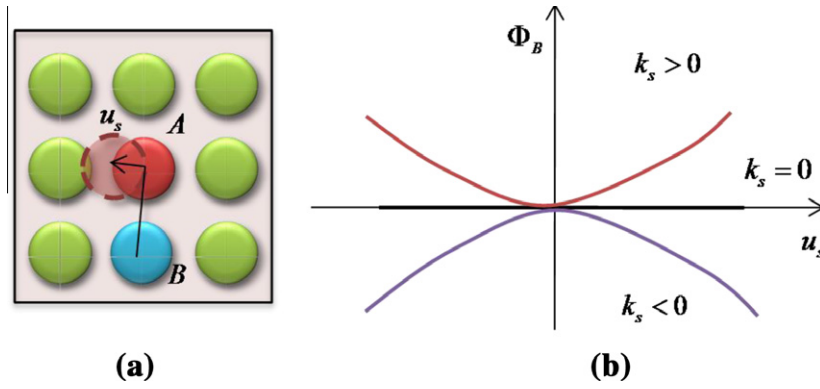


Fig. C1. Physical explanation of the negative stiffness of shear spring (a) Molecular model of material, (b) Potential variation at molecular B.

**Table C1**  
The set of parameters of Finnis–Sinclair potential for silver.

$m$	$n$	$\epsilon$	$\sigma$	$c$	Lattice spacing
6	12	$2.5415 \times 10^{-3}$ eV	4.09 Å	144.41	1.21875 Å

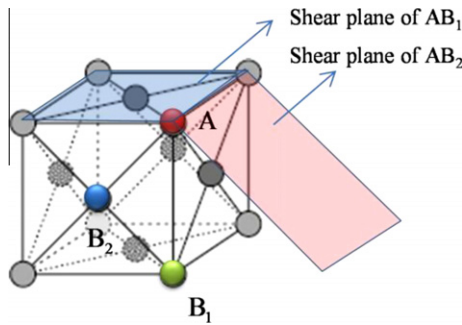


Fig. C2. The cubic face-centred lattice (fcc) structure of silver.

for the plane-stress problems and

$$k_n = \frac{2E}{z^{2D}(1-\nu)(1-2\nu)}$$

$$k_s = \frac{2(1-4\nu)E}{z^{2D}(1+\nu)(1-\nu^2)} \quad (B.9)$$

for the plane-strain problems. Given the geometry data of the lattice spring model,  $\alpha^{2D}$  can be estimated through:

$$\alpha^{2D} = \frac{\sum l_i^2}{A\Delta} \quad (B.10)$$

where  $l_i$  is the original length of the  $i$ th bond. Eqs. (B.8) and (B.9) are used to estimate the two spring stiffnesses of the proposed LSM for numerical simulation of elastic problems.

### Appendix C

#### C.1. Physical interpretation of negative spring

Given a molecular model, as shown in Fig. C1(a),  $\Phi_B(u_s)$  is the potential variation at molecular B versus the displacement of molecular A in the shear direction between A–B. The shape of  $\Phi_B(u_s)$  determines the shear stiffness (see Fig. C1(b)). When the potential function is a constant, the shear stiffness equals to zero, as there is no work needed for displacement. The shear stiffness is positive/negative when the potential function is of an upward/downward bowl shape. Therefore, the proof of the negative shear spring can be based on the potential functions used in MD simulations. It is known that Poisson's ratio of silver is 0.37, which corresponds to negative shear spring stiffness in the DSLM model. The atomic lattice structure of silver is shown in Fig. C2. The Finnis–Sinclair potential proposed by Sutton and Chen (1990) can be used to describe silver, which can be written as

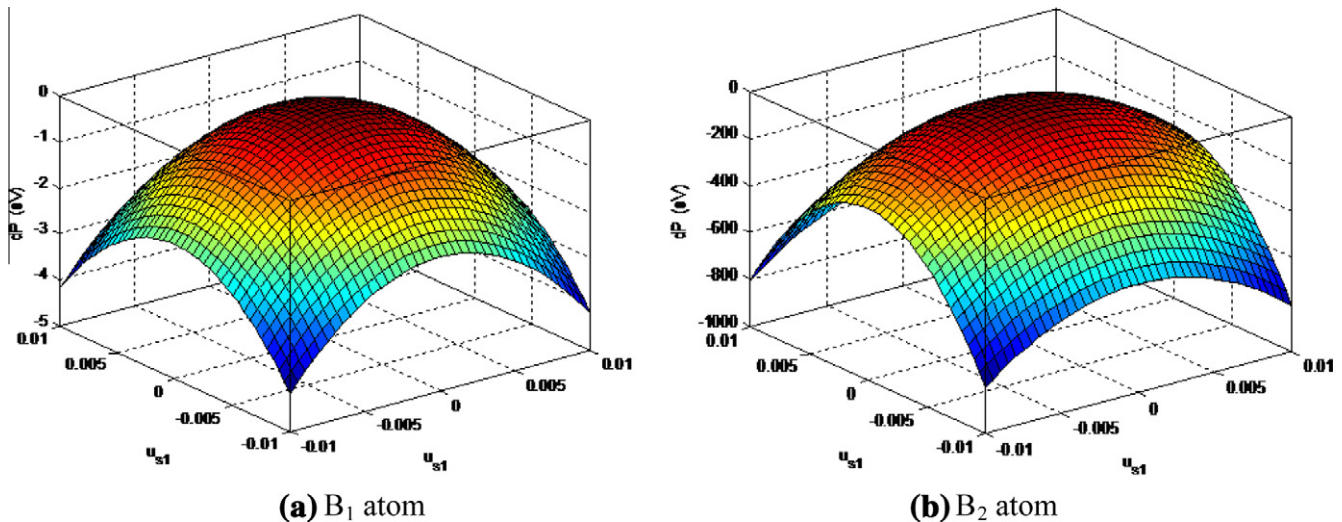


Fig. C3. The variation of potential energy at two different atom positions in the case of silver.

$$P_i = \varepsilon \left( \sum_{\substack{j=1 \\ j \neq i}}^N \left( \frac{\sigma}{r_{ij}} \right)^n - c \sqrt{\sum_{\substack{j=1 \\ j \neq i}}^N \left( \frac{\sigma}{r_{ij}} \right)^m} \right) \quad (\text{C.1})$$

Both repulsive and attractive contributions are included in this potential. The repulsive part is realised by a pair potential, while the attractive part is realised by a many-body potential. The parameters  $n, m, \varepsilon, \sigma$  and  $c$  are material dependent and related to the specific lattice type. The parameter values for silver are given in Table C1.

The potential variation on atom B due to the movement of atom A in different shear planes (see Fig. C2) can be calculated based on Eq. (C.1) and the lattice structure information. The results for silver are shown in Fig. C3. It can be seen that the shape of the variation function is an exact downward bowl shape, which indicates that the shear stiffness is negative. This is consistent with the fact that Poisson's ratio of silver is greater than the critical value (0.25 for 2D and 0.33 for 3D).

## References

- Babuska, I., Melenk, J.M., 1997. The partition of unity method. *Int. J. Numer. Methods Eng.* 40, 727–758.
- Belytschko, T., Black, T., 1999. Elastic crack growth in finite elements with minimal remeshing. *Int. J. Numer. Methods Eng.* 45, 601–620.
- Buxton, G.A., Care, C.M., Cleaver, D.J., 2001. A lattice spring model of heterogeneous materials with plasticity. *Model. Simul. Mater. Sci. Eng.* 9, 485–497.
- Caldarelli, G., Castellano, C., Petr, i A., 1999. Criticality in models for fracture in disordered media. *Physica A: Stati. Mech. Appl.* 270, 15–20.
- Cook, B., Nobel, D., Williams, J., 2004. A direct simulation method for particle-fluid systems. *Eng. Comput.* 21, 151–168.
- Cui, X., Xue, Z., Pei, Y., Fang, D., 2011. Preliminary study on ductile fracture of imperfect lattice materials. *Int. J. Solid Struct.* 48, 3453–3461.
- Cundall, P., Strack, O.D., 1979. A discrete numerical method for granular assemblies. *Geotech.* 29, 47–65.
- Cusatis, G., Bazant, Z.P., Cedolin, L., 2003. Confinement-shear lattice model for concrete damage in tension and compression: I. Theory. *J. Eng. Mech.* 129, 1439–1448.
- Darve, F., Nicot, F., 2005. On incremental non-linearity in granular media: phenomenological and multi-scale views (Part I). *Int. J. Numer. Anal. Methods Geomech.* 29, 1387–1409.
- Farkas, D., Van Swygenhoven, H., Derlet, P.M., 2002. Intergranular fracture in nanocrystalline metals. *Phys. Rev. B* 66, 601011–601014.
- Hahn, M., Wallmersperger, T., Kroplin, B.H., 2010. Discrete element representation of continua: proof of concept and determination of the material parameters. *Comput. Mater. Sci.* 50, 391–402.
- Hahn, M., Schwarz, M., Kroplin, B.H., Wallmersperger, T., 2011. Discrete element method for the thermal field: proof of concept and determination of the material parameters. *Comput. Mater. Sci.* 50, 2771–2784.
- Hasnaoui, A., Van Swygenhoven, H., Derlet, P.M., 2003. Dimples on nanocrystalline fracture surfaces as evidence for shear plane formation. *Science* 300, 1550–1552.
- Hassold, G.N., Srolovitz, D.J., 1989. Brittle fracture in materials with random defects. *Phys. Rev. B* 39, 9273–9281.
- Heermann, H.J., Kertesz, J., De Arcangelis, L., 1989. Fractal shapes of deterministic cracks. *Europhys. Lett.* 10, 147–152.
- Hrennikoff, A., 1941. Solution of problems of elasticity by the framework method. *ASME J. Appl. Mech.* 8, A619–A715.
- Kazerani, T., Zhao, G.F., Zhao, J., 2010. Dynamic fracturing simulation of brittle material using the Distinct Lattice Spring Model (DLSM) with a full rate-dependent cohesive law. *Rock Mech. Rock Eng.* 43, 717–726.
- Kozicki J., 2007. Application of discrete models to describe the fracture process in brittle materials, PhD Thesis. Gdansk University of Technology, Poland.
- Kwapinska, M., Saage, G., 2008. Continuous versus discrete modelling of heat transfer to agitated beds. *Powder Technol.* 181, 331–342.
- Lilliu, G., van Mier, J.G.M., 2003. 3D lattice type fracture model for concrete. *Eng. Fract. Mech.* 70, 927–941.
- Ma, H.S., Yin, L.J., Ji, H.G., Zhao, G.F., 2011. Modelling dynamic crack propagation by Distinct Lattice Spring Model. *Proc. ICADD10 Analysis of Discontinuous Deformation: Advan. Discontin. Num. Meth. Appl. Geomech. Geoen.*, 321–326.
- Marsden, J.E., Hughes, T.J.R., 1983. *Mathematical Foundations of Elasticity*. Prentice-Hall: Englewood Cliffs, New Jersey.
- Mustoe, G.G.W., 1992. Generalized formulation of the discrete element method. *Eng. Comput.* 9, 181–190.
- O'Brien, G.S., 2008. Discrete visco-elastic lattice methods for seismic wave propagation. *Geophys. Res. Lett.* 35, L02302. <http://dx.doi.org/10.1029/2007GL032214>.
- Ostoja-Starzewski, M., Sheng, P.Y., Jasiuk, I., 1977. Damage patterns and constitutive response of random matrix-inclusion composites. *Eng. Fract. Mech.* 58, 581–606.
- Parisi, A., Caldarelli, G., 2000. Self-affine properties of fractures in brittle materials. *Physica A: Stati. Mech. Appl.* 280, 161–165.
- Potyondy, D.O., Cundall, P.A., 2004. A bonded-particle model for rock. *Int. J. Rock Mech. Min. Sci.* 41, 1329–1364.
- Rosch, F., Rudhart, C., Roth, J., Trebin, H.R., Gumbsch, P., 2005. Dynamic fracture of icosahedral model quasicrystals: a molecular dynamics study. *Phys. Rev. B* 72, 1–9.
- Sakaguchi, H., Muhlhaus, H.B., 2000. Hybrid modelling of coupled pore fluid-solid deformation problems. *Pure App. Geophys.* 157, 1889–1904.
- Schlangen, E., Garboczi, E.J., 1997. Fracture simulations of concrete using lattice models: computational aspects. *Eng. Fract. Mech.* 57, 319–332.
- Sutton, A., Chen, J., 1990. Long-range Finnis-Sinclair potentials. *Philos. Mag. Lett.* 61, 139C146.
- Tadmor, E.B., Ortiz, M., Phillips, R., 1996. Quasicontinuum analysis of defects in solids. *Philos. Mag. A* 73, 1529–1593.
- Wang, G., Al-Ostaz, A., Cheng, A.H.D., Mantena, P.R., 2009. Hybrid lattice particle modeling: theoretical considerations for a 2D elastic spring network for dynamic fracture simulations. *Comput. Mater. Sci.* 44, 1126–1134.
- Wang, Y.C., Abe, S., Latham, S., Mora, P., 2006. Implementation of Particle-scale Rotation in the 3-D Lattice Solid Model. *Pure. Appl. Geophys.* 163, 1769–1785.
- Williams, J.R., Mustoe, G.G.W., 1987. Modal methods for the analysis of discrete systems. *Comput. Geotech.* 4, 1–19.
- Yu, A.B., 2004. Discrete element method An effective way for particle scale research of particulate matter. *Eng. Comput.* 21, 205–214.
- Zhang, Z.N., Ge, X.R., 2005. Micromechanical consideration of tensile crack behavior based on virtual internal bond in contrast to cohesive stress. *Theor Appl Fract Mech* 43, 342–359.
- Zhao, G.F., Fang, J., Zhao, J., 2011. A 3D distinct lattice spring model for elasticity and dynamic failure. *Int. J. Numer. Anal. Methods. Geomech.* 35, 859–885.
- Zhao G.F., 2010. Development of micro-macro continuum-discontinuum coupled numerical method. PhD Thesis. EPFL, Switzerland.
- Zhao, G.F., Ma, G.W., Zhang, H.H., Zhao, J., 2010. A numerical manifold method for plane micropolar elasticity. *Int. J. Comput. Meth.* 7, 151–166.